ACS NANO
Cite This: ACS Nano 2019, 13, 14468−14476
www.acsnano.org

ARTICLE

Band-Structure Spin-Filtering in Vertical Spin Valves Based on Chemical Vapor Deposited WS_2

Victor Zatko,*,† Marta Galbiati,† Simon Mutien-Marie Dubois,†,§ Mauro Och,⊥ Pawel Palczynski,⊥ Cecilia Mattevi,⊥ Pierre Brus,†,‡ Odile Bezencenet,‡ Marie-Blandine Martin,† Bernard Servet,‡ Jean-Christophe Charlier,§ Florian Godel,† Aymeric Vecchiola,† Karim Bouzehouane,† Sophie Collin,† Frédéric Petroff,† Bruno Dlubak,*,† and Pierre Seneor*,†

†Unité Mixte de Physique, CNRS, Thales, Univ Paris-Sud, Université Paris-Saclay, 91767 Palaiseau, France
‡Thales Research and Technology, 1 avenue Augustin Fresnel, 91767 Palaiseau, France
§Institute of Condensed Matter and Nanosciences, Université catholique de Louvain, B-1348 Louvain-la-Neuve, Belgium
⊥Department of Materials, Imperial College London, Exhibition Road, London SW7 2AZ, U.K.

ABSTRACT: **We report on spin transport in WS_2-based 2D-magnetic tunnel junctions (2D-MTJs), unveiling a band structure spin filtering effect specific to the transition metal dichalcogenides (TMDCs) family. WS_2 mono-, bi-, and trilayers are derived by a chemical vapor deposition process and further characterized by Raman spectroscopy, atomic force microscopy (AFM), and photoluminescence spectroscopy. The WS_2 layers are then integrated in complete $Co/Al_2O_3/WS_2/Co$ MTJ hybrid spin-valve structures. We make use of a tunnel Co/Al_2O_3 spin analyzer to probe the extracted spin-polarized current from the WS_2/Co interface and its evolution as a function of WS_2 layer thicknesses. For monolayer WS_2, our technological approach enables the extraction of the largest spin signal reported for a TMDC-based spin valve, corresponding to a spin polarization of P_{Co/WS_2} = 12%. Interestingly, for bi- and trilayer WS_2, the spin signal is reversed, which indicates a switch in the mechanism of interfacial spin extraction. With the support of *ab initio* calculations, we propose a model to address the experimentally measured inversion of the spin polarization based on the change in the WS_2 band structure while going from monolayer (direct bandgap) to bilayer (indirect bandgap). These experiments illustrate the rich potential of the families of semiconducting 2D materials for the control of spin currents in 2D-MTJs.**

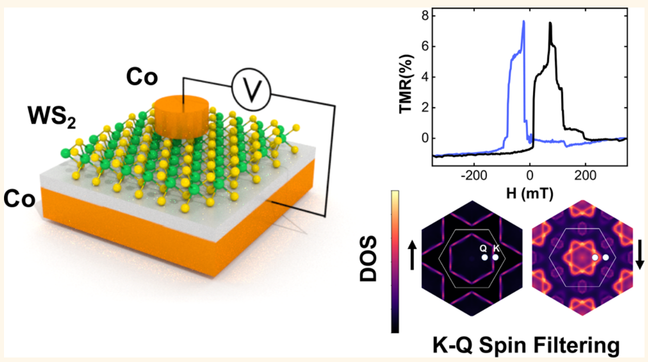

KEYWORDS: *tungsten disulfide, 2D, semiconductor, spin filtering, spintronics, magnetic tunnel junction*

Prototypical in spintronics, magnetic tunnel junctions (MTJs) are exploited in hard drives read heads, MRAMs,[1−4] and more recently highlighted beyond spin logics[5,6] for neuromorphic and stochastic calculation, which may prove as an alternative to quantum calculation.[7−9] They are schematically made of two ferromagnets acting as spin polarizer and analyzer separated by an ultrathin tunnel barrier. The spin polarization of the current tunneling through the junction essentially depends on the specificities of the electronic states at the ferromagnets interfaces.[10] Thus, even slight physical modifications of the interfaces might lead to significant changes in the electrical and spin behavior of the junctions. It is thus envisioned that spin current properties might be controlled and tailored by the insertion of atomically thin 2D materials in spin valves. In this direction, while very recent, the introduction of 2D materials in MTJs has already shown some promising properties (atomic thickness control, spin filtering, perpendicular magnetic anisotropy, spin−orbit torques modulation, *etc.*).[11−15] Graphene, and later the 2D insulator h-BN (6 eV bandgap), has been the first 2D material to be studied for vertical spin transport in MTJs.[16−22] Strikingly, in line with theoretical expectation,[23] it was quickly shown that a "bulk" K-point spin filtering was occurring in graphene-based MTJs with the creation of an insulating majority spin channel. The recent advent of 2D semiconductors has opened opportunities for further tailoring

Received: October 16, 2019
Accepted: November 19, 2019
Published: November 27, 2019

DOI: 10.1021/acsnano.9b08178
ACS Nano 2019, 13, 14468−14476

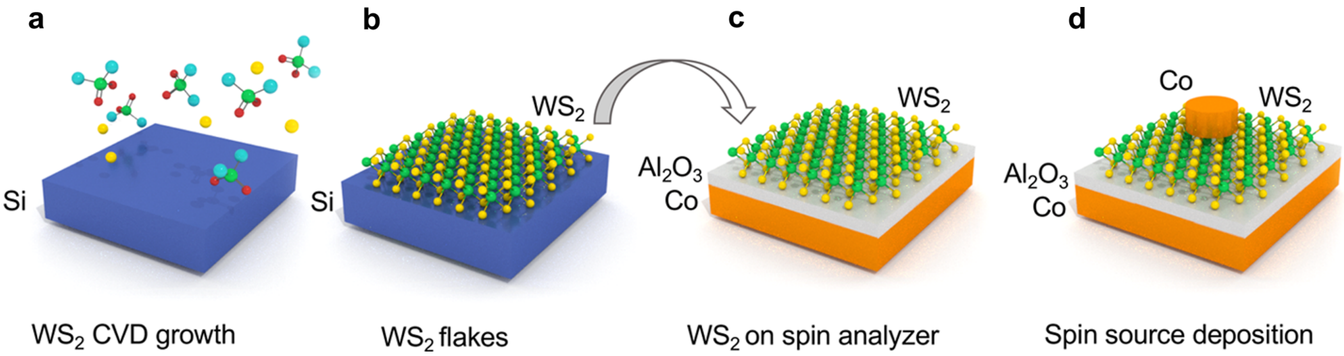

Figure 1. Schematics of the fabrication steps of the CVD WS_2-based magnetic tunnel junctions (MTJs). (a) CVD process leading to the growth of WS_2 flakes on SiO_2/Si substrate (see details in Methods). (b, c) Transfer of the flakes on a reference Co/Al_2O_3 spin analyzer. (d) Deposition of a top Co spin polarizer electrode.

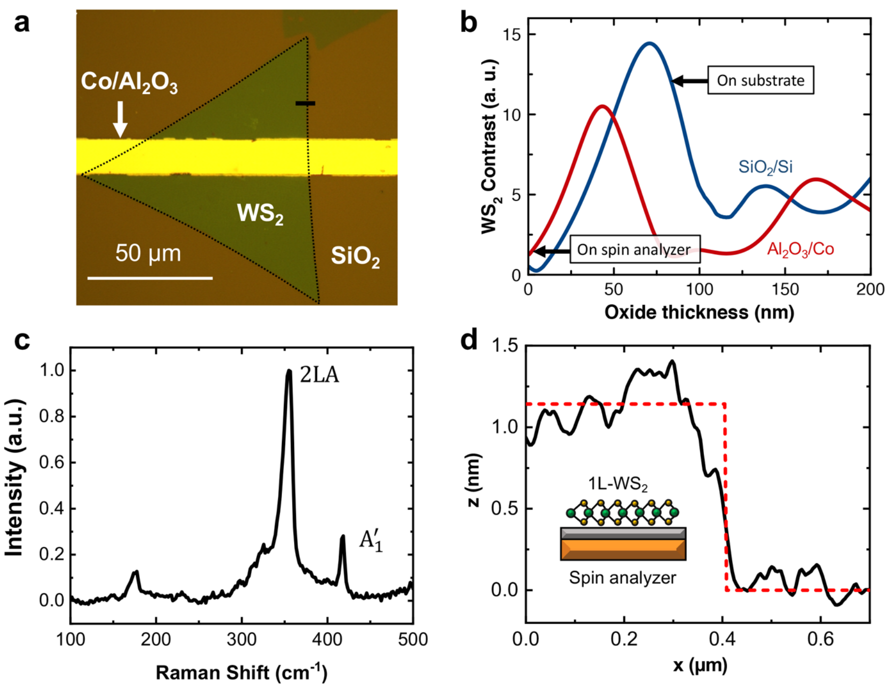

Figure 2. Characterization of monolayer WS_2 flake A. (a) Optical image of the flake transferred on top of the spin analyzer. Black contour as guide to the eye and black bar corresponds to AFM profile. (b) Calculated WS_2 contrast on SiO_2/Si and Al_2O_3/Co as a function of the oxide thickness, predicting the observed WS_2 strong contrast on the SiO_2(90 nm)/Si substrate and low contrast on our bottom spin analyzer electrode Al_2O_3(1 nm)/Co. (c) Raman spectrum measured on the flake showing a typical WS_2 monolayer signature. (d) Tapping-mode AFM on a step of the WS_2 flake confirming its monolayer thickness.

those spintronics properties.[11,24] Among them, the transition metal dichalcogenides (TMDCs) family offers a wide landscape of materials with varied transport properties due to changes of the band structure depending on their atomic composition and thickness.[25−32] Initial focus has been centered on MoS_2,[33−40] and other promising TMDCs, such as WS_2, have been studied for spintronics devices.[41−47] The broad ranges of band structures and transport properties of TMDCs, including field effect spin-split band structures,[27,30,32,48−50] make them promising candidates for spintronics applications.[51,52] Nevertheless, integration issues with ferromagnets have so far hampered their full exploitation in magnetic tunnel junctions:[11] their properties have barely been unraveled in experimental vertical spin structures.

In this paper, we report on spin transport in magnetic tunnel junctions based on atomically thin chemical vapor deposition (CVD) grown WS_2 layers. The use of a reference Co/Al_2O_3 spin analyzer unveils the fundamental impact of WS_2 band structure, controlled by its thickness, on the polarizations of extracted spin currents. CVD grown WS_2 flakes are integrated in spin valve structures (Figure 1) and analyzed by atomic force microscopy (AFM), Raman spectroscopy, and photoluminescence (PL) (Figure 2). Magneto-transport measurements are performed showing a spin polarization of the FM/WS_2 interface of up to 12%, corresponding to the highest value reported to date in 2D semiconductor-based MTJs (Figure 3). The study of 1, 2, and 3 layers thick WS_2 in these junctions (Figure 4) allows us to pinpoint a specific thickness dependent spin-valve effect, highlighting an abrupt inversion of the spin polarization for junctions with two and more WS_2 layers (Figure 5). Supported by *ab initio* calculations, we propose a crystal momentum selection model to interpret the thickness dependence of the Co/WS_2 interface. The WS_2 monolayer exhibits a direct bandgap at the K-points of its Brillouin zone

DOI: 10.1021/acsnano.9b08178
ACS Nano 2019, 13, 14468−14476

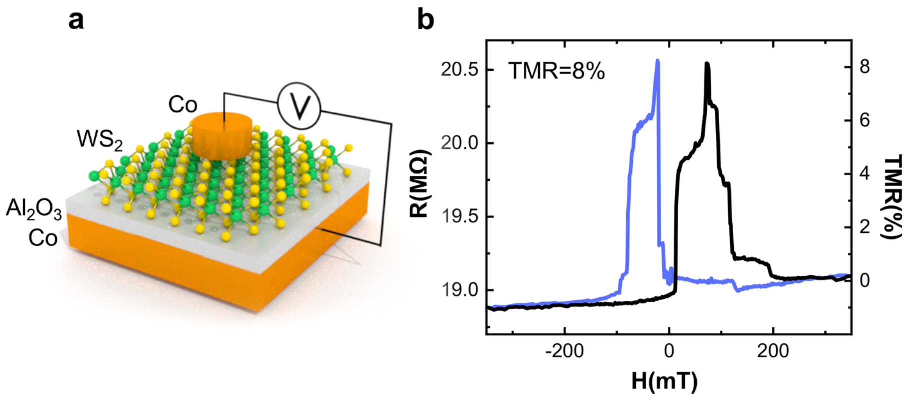

Figure 3. Magneto-transport measurements of the spin current extracted from monolayer WS_2/Co interface. (a) Scheme of the Co/Al_2O_3/1L-WS_2/Co MTJ. (b) Resistance versus magnetic field at T = 4K and V = 20 mV with a measured TMR = 8%. This corresponds to a state-of-the-art spin polarization of about $P_{WS_2/Co}$ = 12% in our system.

corresponding to majority spins pockets of the Co electrode. In stark contrast, the thicker layers have an indirect bandgap between the highest energy point of the valence band at the Γ-point and the lowest energy point of the conduction band located between the Γ-point and the K-point, corresponding to minority spins of Co. The evolution of the WS_2 band structure with thickness is thus shown to lead to a sharp inversion of the spin polarization (Figure 6), with promising perspectives for the tailoring of spintronics devices using 2D materials.

RESULTS AND DISCUSSION

Figure 1 shows the fabrication process leading to the 2D WS_2-based magnetic tunnel junctions. To gain access to large WS_2 flakes, we employed CVD grown material (Figure 1a,b). The process follows the procedure reported by Reale *et al.*[53] It is based on the use of H_2WO_4 precursor mixed with NaCl reacting with S atoms from sulfur powder placed upstream in the furnace for the growth of large ∼50 μm flakes of WS_2 on SiO_2/Si substrates (see Methods for further details). After this growth, the WS_2 is transferred on top of a Co/Al_2O_3 spin analyzer (Figure 1b,c and Figure 2a) via a PMMA-assisted method described in ref 53 to probe its spin transport properties. However, we note that the contrast of the atomically thin flakes on Co/Al_2O_3(1 nm) is extremely low (Figure 2b); this would make them particularly difficult to spot during device fabrication. In this regard, we have designed a bottom Co/Al_2O_3 electrode narrow enough to let the large WS_2 flakes partially lie on a SiO_2 (90 nm)/Si substrate where their contrast is high (as shown on Figure 2b). The bottom electrode is defined by a laser lithography step on top of the SiO_2/Si wafer, with the Co(50 nm)/Al_2O_3(1 nm) stack being deposited by sputtering. Co/Al_2O_3 electrodes spin properties have been largely explored in the literature.[54,55] More specifically, we made use here of a lower electrode that we have already used and characterized as a tunnel spin analyzer, allowing us to use it as a reference system.[56,57] Al_2O_3 plays the role of a tunnel barrier for the spin analyzer; furthermore, it also prevents Co from oxidation allowing manipulation in ambient conditions for flake transfer. This process leads to the definition of a Co/Al_2O_3/WS_2 heterostructure.

We first focus on a 50 μm wide WS_2 flake, which is transferred on top of the Al_2O_3/Co electrode (flake A). An optical image of flake A is shown in Figure 2a. The contrast of the flakes on SiO_2/Si depends on the number of atomic layers. We have chosen flake A in particular because of its low contrast on the substrate, potentially corresponding to an atomically thin flake. To confirm this initial observation, Raman spectroscopy is performed with a 514 nm laser. A typical spectrum measured for flake A is shown in Figure 2c. The two dominating peaks observed are attributed to the in-plane 2LA (overlapped with E^1_{2g}) and the out-of-plane A'_1 modes.[58] Interestingly, the ratio of these peaks intensities ($I_{2LA}/I_{A'_1}$) allows us to determine the number of layers of the flakes (with atomic precision at least up to 3 WS_2 layers).[58] Flake A shows a 2LA mode intensity more than twice that of the A'_1 mode, which is the signature of a monolayer of WS_2. Further characterization by AFM is carried as shown in Figure 2d, confirming its single layer thickness,[58] in line with the Raman measurements.

We thus fabricate a spin valve device based on the identified monolayer WS_2 flake deposited on the Al_2O_3/Co spin analyzer. To complete our device and define the top ferromagnetic electrode, a circular microjunction is patterned on top of the flake with another step of lithography as shown in Figure 1d. Then evaporation is used to deposit a Co film (15 nm) capped with a layer of Au (80 nm), resulting in a ∼1 μm^2 Co spin source (top electrode) centered on the ∼50 μm wide WS_2 flake above the Co/Al_2O_3 spin analyzer. Our evaporation process approach, being a soft deposition method that avoids material damage, has previously demonstrated state of the art results for device integration of 2D materials.[59,60] Finally, the junction is electrically contacted to a ceramic chip. In this complete WS_2 device, the Co/Al_2O_3 electrode acts as a spin analyzer of the current extracted from Co/WS_2 (Figure 3a).

In Figure 3b, we show magneto-transport measurements for a MTJ based on a single WS_2 layer (flake A) at 4K. We plot the resistance versus magnetic field to extract the TMR spin signal, where $TMR = \frac{R_{AP} - R_P}{R_P}$ with R_P and R_{AP} the resistances of the parallel and antiparallel configurations of the magnetizations of the two ferromagnets, respectively. We measure a TMR spin signal of about 8%, above the state of the art for 2D semiconductor-based MTJs and more than one order of magnitude larger than for previous WS_2-based MTJs.[41] This result comforts our integration approach, which seeks to preserve the chemical state of the FM interfaces free from oxidation by the use of a high quality tunnel barrier.[61] We note that, in our devices, the TMR showed only monotonous dependencies with bias, a typical behavior of tunnel vertical spin valves.

DOI: 10.1021/acsnano.9b08178
ACS Nano 2019, 13, 14468−14476

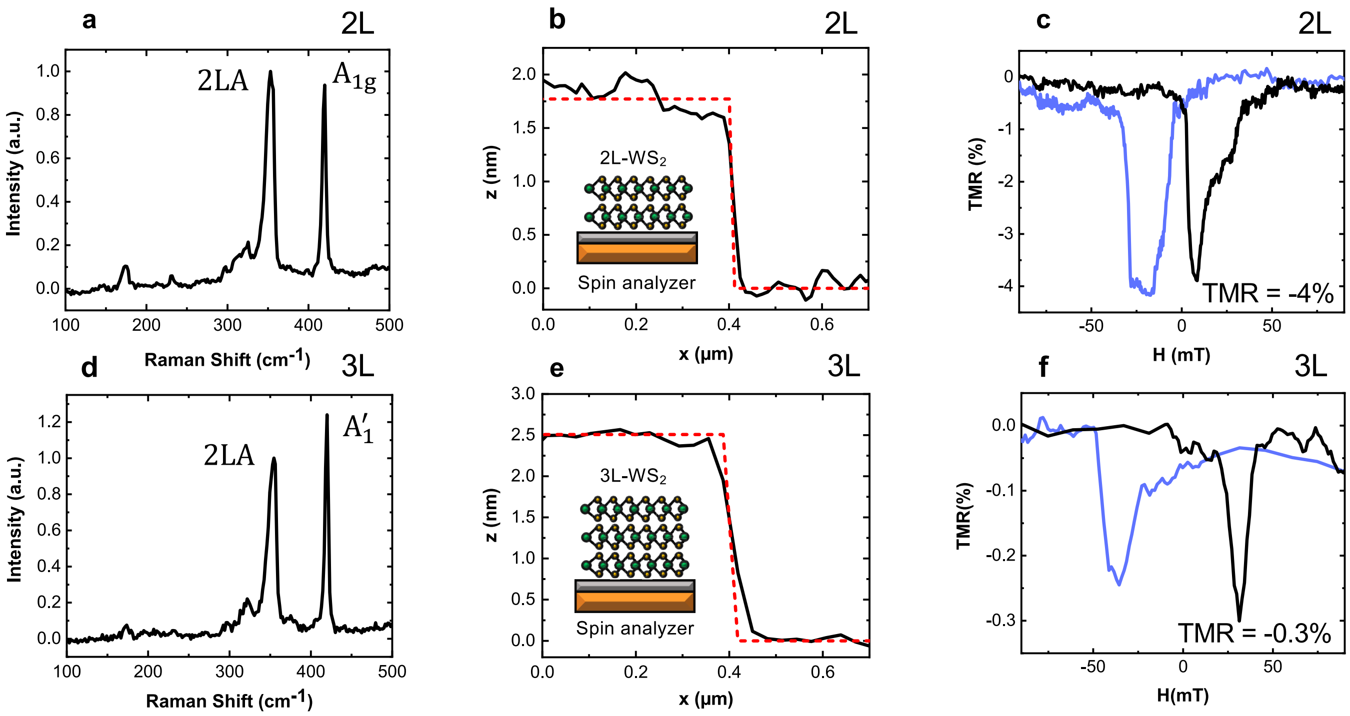

Figure 4. Characterization of bilayer WS_2 (flake B) and trilayer WS_2 (flake C). (a, d) Raman measurement of flake B and C, respectively. (b, e) Tapping-mode AFM on flake B and C. Flake B is thus shown to be a bilayer and flake C a trilayer. Both flakes are integrated in a complete MTJ, allowing to probe spin transport across these structures. (c, f) Resistance versus magnetic field at 4K for the bi- (20 mV) and trilayers (10 mV) based $Co/Al_2O_3/WS_2/Co$. A striking inversion of the spin signal is noted for these multilayer flakes.

Since the CVD approach is able to produce large flakes of different well-defined thicknesses,[50,58] the exact same characterization and fabrication procedure has been applied to flakes that appear optically with a stronger contrast, implying a larger number of layers (flake B and flake C). The Raman spectrum measured on flake B (Figure 4a) shows almost the same intensity for both 2LA and A_{1g} modes (note that A_{1g} mode corresponds to the A_1' peak of the monolayer as for an odd number of layers the inversion symmetry is broken and the labeling A_1' is used, while for an even number of layers the out-of-plane mode becomes A_{1g}).[62,63] The ratio $I_{2LA}/I_{A_{1g}}$ gives a value of 1.1 as expected for a bilayer.[58] In the case of flake C, the Raman spectrum is characteristic of a trilayer flake with the 2LA mode being slightly weaker than the A_1' mode and $I_{2LA}/I_{A_1'} = 0.8$ (Figure 4d). In Figure 4b and e, AFM profiles are reported as well, showing that flake C is one layer thicker than flake B itself being one layer thicker than flake A. These different characterizations (optical, Raman, AFM) show that flake B and C, respectively, correspond to bi- and trilayers.[58]

The further integration of flake B and C in $Co/Al_2O_3/WS_2/Co$ stacks leads to MTJs based on two and three layers thick WS_2 flakes, respectively. In Figure 4c and f, we plot the magneto-transport measurements obtained on those bi- and trilayers WS_2 MTJs. We observe TMR signals for each case. Interestingly, when compared with the monolayer case, the sign and the amplitude of the TMR depend on the thickness of WS_2. In particular, for bi- and trilayers, the TMR signal becomes negative. We note that this sign inversion with thickness has been reliably repeated with other junctions, with similar spin signal amplitudes. This can be further analyzed as in the fabricated devices where we made use of a reference Co/Al_2O_3 spin analyzer with a known spin polarization P_{ref}. This enables us to directly extract the spin polarization of the WS_2/Co interface. Indeed, using a phenomenological Jullière's model,[64] we obtained $TMR = \frac{2P_{ref}P_{WS_2/Co}}{1 - P_{ref}P_{WS_2/Co}}$ with $P_{WS_2/Co}$ the spin polarization of the WS_2/Co interface. With P_{ref} being known ($P_{ref} = 32\%$),[56,57] we can extract $P_{WS_2/Co}$ from the TMR measurement as a function of WS_2 thickness: $P_{1L\text{-}WS_2/Co} = +12\%$, $P_{2L\text{-}WS_2/Co} = -6\%$, and $P_{3L\text{-}WS_2/Co} = -0.5\%$.

A strong thickness dependence of the spin signal is thus observed, with a striking sign reversal for multilayers compared to the monolayer case as shown in Figure 5a. Interestingly, a drastic change in the band structure of WS_2 is known to arise when changing its thickness: the bandgap of WS_2 goes from direct for a monolayer to indirect for larger thicknesses (Figure 5c,d).[27,30,32,48] This is confirmed in the case of flakes A, B, and C by a PL study probing their actual bandgap properties. As expected from the literature,[65] we observe an evolution of the PL signal with flakes thicknesses. The PL signal measured for mono-, bi-, and trilayer flakes is presented in Figure 5b. For the monolayer, only one peak is observed corresponding to the direct bandgap (transition K−K). In contrast, for the bilayer flake, two peaks are observed, with the additional peak arising from the dominant contribution of the indirect bandgap (transition Γ−Q). In the case of the trilayer, mostly one peak is observed as the direct bandgap related peak is almost quenched, leaving just the contribution of the indirect bandgap. The modulation of spin polarization could be related to the change in the fundamental band structure of the WS_2 layers. As shown in Figure 5c and d, the minima of its conduction band, initially located at the corner of the Brillouin zone (K-point) for the monolayer, shift toward the center of

DOI: 10.1021/acsnano.9b08178
ACS Nano 2019, 13, 14468−14476

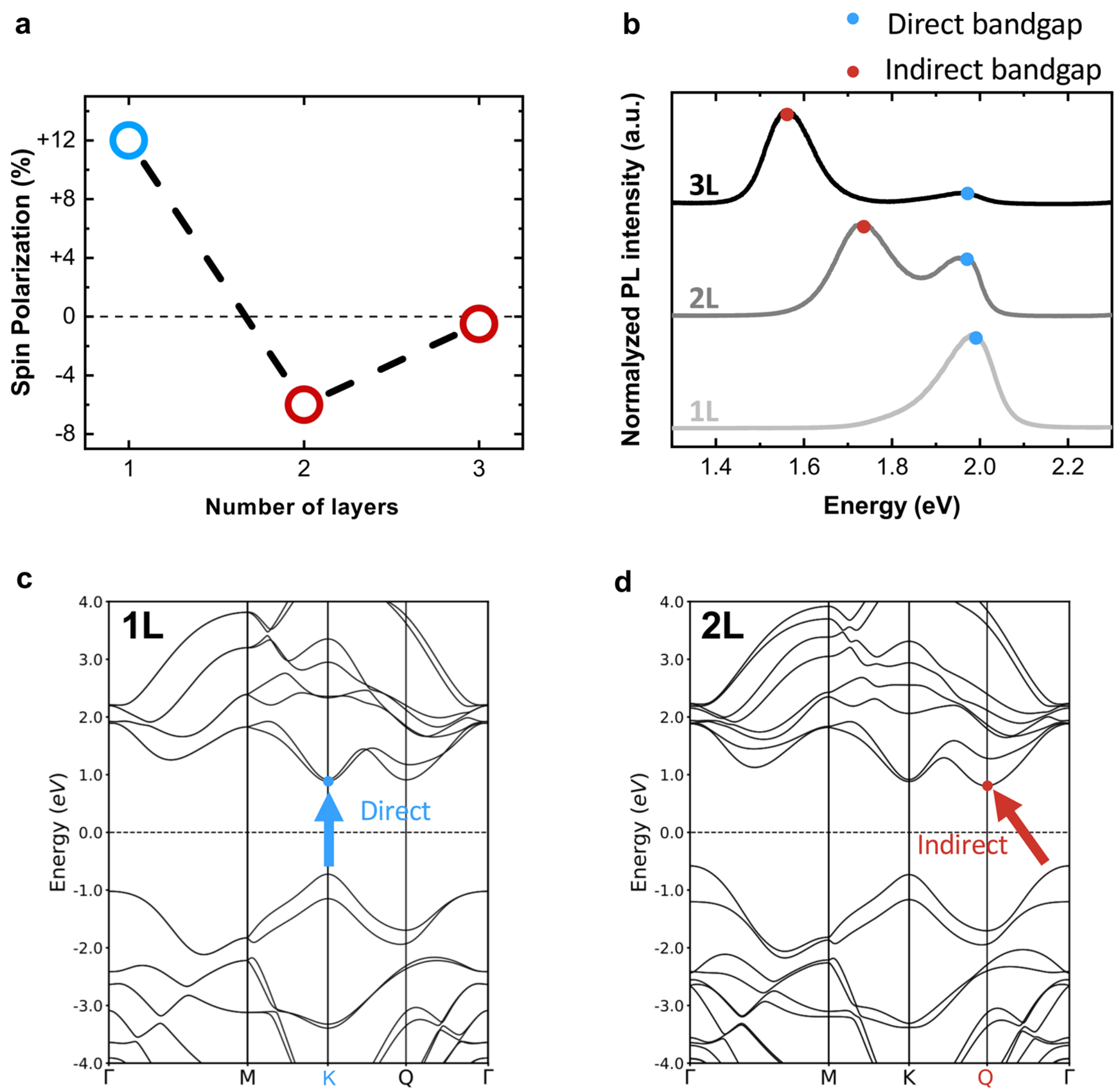

Figure 5. Effect of the WS_2 thickness on spin transport: photoluminescence and band structure. (a) Spin polarization at the WS_2/Co interface versus WS_2 thickness, extracted thanks to the use of a reference Co/Al_2O_3 spin analyzer. The large positive spin polarization of the monolayer case is shown to be inverted when additional layers are present (bi- and trilayer cases). It is also observed that the amplitude of the spin polarization is decreasing with the WS_2 thickness. (b) Photoluminescence of WS_2 for mono-, bi-, and trilayers. Only one peak appears for a monolayer, corresponding to the predicted direct bandgap, and vanishes as the thickness increases. The peak corresponding to the expected indirect bandgap appears for a bilayer and dominates for trilayers. (c, d) Band structure of respectively monolayer and bilayer WS_2, showing a transition from direct (1L) to indirect (2L) bandgap.

the Brillouin zone (Q-point) upon addition of supplementary layers directly impacting spin selection at the interface.

We illustrate the proposed spin selection mechanism in Figure 6 with a toy model derived from the band structures of bulk hcp-Co and freestanding WS_2 mono- and bilayers. The ***k***-resolved spin-dependent density of states at Fermi level is computed for bulk hcp-Co and integrated over the ⟨*0001*⟩ axis (*i.e.*, the direction of transport), resulting in the $\boldsymbol{k}_{\perp}$-space maps of Figure 6. The conduction bands minima of WS_2 monolayer and bilayer (which are similar for thicker flakes up to bulk) are added on these reciprocal space maps accounting for the difference of lattice parameters between hcp-Co and free-standing WS_2 mono/bilayers. These minima correspond to regions of $\boldsymbol{k}_{\perp}$-space where transport is favored. Interestingly, for monolayer WS_2, transport is favored in $\boldsymbol{k}_{\perp}$-space regions within the first Brillouin zone of Co where majority spin carriers dominate the DOS, hence corresponding to a positive polarization of the interface. This is reminiscent of the bulk K-point spin filtering effect previously predicted[23] and observed[11,66] in graphene-based MTJs. In the case of graphene, the spin polarization is expected to be monotonous with the number of stacked layers, as conduction remains correlated to K-point in reciprocal space for all thicknesses. In contrast, we can clearly observe here that the thickness of WS_2 affects more dramatically the spin polarization extracted from cobalt. The switch from direct (K−K) to indirect (Γ-Q) gap corresponds to the selection of different pockets of spin-polarized electrons in Co. The case of bilayer WS_2 is inverted compared to monolayer in terms of spin polarization as $\boldsymbol{k}_{\perp}$-space regions where minority spin carriers dominate are selected. This is in-line with the measured dramatic change of spin signal occurring in devices by simply adding one WS_2 layer to the monolayer case. Though Figure 6 provides a helpful picture for the description of the $\boldsymbol{k}_{\perp}$-space spin-selection mechanism, we

DOI: 10.1021/acsnano.9b08178
ACS Nano 2019, 13, 14468−14476

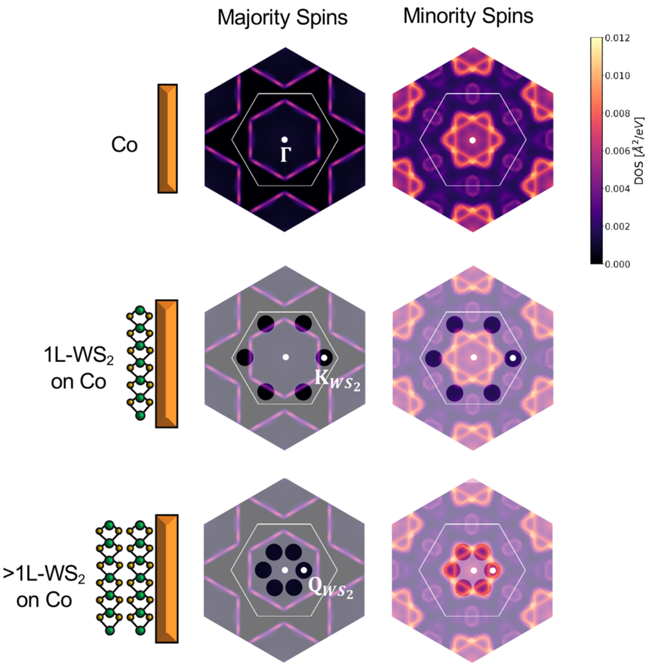

Figure 6. Effect of the WS_2 thickness on the spins extracted from Co. The *k*-resolved spin-dependent density of states (DOS) at Fermi level is computed from first-principles for bulk hcp-Co and integrated over the ⟨*0001*⟩ axis, resulting in the depicted $k_\perp$-resolved DOS maps for majority spins and minority spins (first row). The holes in the shading represent the energy minima of the conduction band of WS_2 for monolayer (second row) and bilayer (third row) overlapping, highlighting the regions in reciprocal space where transport is favored within the first Brillouin zone of Co. It appears that depending on the WS_2 thickness, different pockets of electrons are selected from the Fermi surface of Co, corresponding to different spin polarizations of the transport channels.

emphasize that this mechanism is certainly more complex than the model presented here. For a given sample, the actual $k_\perp$-space map will depend on the details of the interface structure, extending over many Brillouin-zones depending on the relative orientations and strain of bulk Co and WS_2 multilayers. Besides, the band structure of monolayer WS_2 should in some case be also affected by the neighboring ferromagnet. This has been for instance observed for h-BN/Co with diverse "spinterfaces" depending on coupling strength.[20] However, the main point remains to note that a change in the band structure of our TMDC, controlled by the thickness, can have a sizable effect on spin transport across the junction, here shown to even be able to fully reverse the spin filtering polarization. The picture proposed here outlines the tunable spin filtering properties of WS_2, and TMDCs in general as the thickness dependent gap is a common feature to this 2D materials family.

Finally, we discuss the quenching of the spin signal amplitude observed as we increase the WS_2 thickness. While it is probable that thick flakes enhance the probability of spin scattering, in turn limiting the extracted spin signal, the effect is surprisingly abrupt for what could be expected in the case of a purely vertical transport. As previously shown by Galbiati *et al.*,[34] this can be explained by the observation that in TMDC materials the current diffuses in the plane of the layers even with a bias applied perpendicular to the junction. Thus, for thick flakes, we expect a depolarization arising essentially from the current flowing in the plane of the 2D material, and not from the out-of-plane current. Interestingly, as measured in our devices, this problematic is certainly attenuated in the case of mono- and bilayers where lateral diffusion is more mitigated by competition with vertical transport.

CONCLUSION

In conclusion, this study explores spin transport in vertical spin valves based on CVD grown WS_2 flakes. Thanks to our specific device fabrication approach that prevents deleterious oxidation, the extracted spin signal is shown to raise above state of the art for 2D semiconductors-based MTJs. We reach a spin polarization for the Co/WS_2 monolayer interface of about 12%. Moreover, we emphasize the role of the WS_2 thickness and band structure on spin transport in MTJs. WS_2 is shown to behave as a K−Q-points spin filter, expanding the K-point spin filtering effect of graphene usually discussed.[23] The spin polarization sign/amplitude can thus be expected to be controlled by direct (monolayer) versus indirect (bi- and trilayers) WS_2 bandgap, a characteristic that should be common to many TMDCs. Our work thus highlights the potential of the rich TMDC family of 2D materials to control spin transport properties in 2D-MTJs.[11]

METHODS

WS_2 CVD Growth. Commercial H_2WO_4 and NaCl powders are mixed (1:1 in weight) in an alumina boat and placed in a tubular furnace with a dual temperatures controlled system along with an alumina crucible filled with sulfur powder placed upstream. In the presence of a carrier gas (100 sccm of highly pure Ar at a pressure of 1.4 mbar for 15 min), the W-containing crucible is heated at 850 °C, whereas the sulfur powders are heated up to only 125 °C. Tungstic acid and salt react at high temperature to form volatile oxychloride species ($WOCl_4$/WO_2Cl_2) that react with S to form WS_2 atomically thin flakes on a SiO_2(285 nm)/Si substrate that was placed downstream at 850 °C.

Device Fabrication. Bottom electrodes of the WS_2-based 2D-MTJ spin valves are designed by laser lithography using SPR 700 resist on SiO_2(90 nm)/Si substrate. The Co(50 nm)/Al_2O_3(1 nm) tunnel spin analyzers are deposited by sputtering. The CVD grown WS_2 flakes are transferred on top. Additional laser lithography and evaporation steps lead to the fabrication of gold-capped Co(15 nm) spin sources on top of the flakes and to the definition of final circular microjunctions.

First-Principles Calculations. All first-principles calculations have been performed in the framework of the density functional theory (DFT) using the projector augmented wave (PAW) method as implemented within VASP[67,68] with an energy cutoff of 400 eV for the plane-wave expansion. Exchange and correlation are described within the generalized gradient approximation using the Perdew−Burke−Ernzerhof (PBE) parametrization.[69]

AUTHOR INFORMATION

Corresponding Authors

*E-mail: victor.zatko@cnrs-thales.fr.
*E-mail: bruno.dlubak@cnrs-thales.fr.
*E-mail: pierre.seneor@cnrs-thales.fr.

ORCID

Victor Zatko: 0000-0002-2475-8866
Cecilia Mattevi: 0000-0003-0005-0633
Florian Godel: 0000-0003-1741-2741
Bruno Dlubak: 0000-0001-5696-8991

Notes

The authors declare no competing financial interest.

DOI: 10.1021/acsnano.9b08178
ACS Nano 2019, 13, 14468−14476

ACKNOWLEDGMENTS

We acknowledge financial support from the European Commission through H2020 Future and Emerging Technologies Graphene Flagship (Grants Nos. 696656 and 785219). This research is supported by a public grant overseen by the French National Research Agency (ANR) as part of the "Investissements d'Avenir" program (Labex NanoSaclay, reference: ANR-10-LABX-0035). S.M.-M.D. and J.-C.C. acknowledge the National Fund for Scientific Research of Belgium [F.R.S.-FNRS] and the Research Concerted Action on 3D Nanoarchitecturing of 2D crystals (No. 16/21-077) for financial support. Computational resources were provided by the supercomputing facilities of UCLouvain (CISM) and the "Consortium des Équipements de Calcul Intensif en Fédération Wallonie-Bruxelles" (CECI). C.M. would like to acknowledge the EPSRC award, EP/M022250/1, the EPSRC-Royal Society Fellowship Engagement Grant EP/L003481/1, the Research Fellows Enhancement Award 2017 RGF\EA \180090, and the award of a Royal Society University Research Fellowship both by the U.K. Royal Society.

REFERENCES

(1) Chappert, C.; Fert, A.; Nguyen Van Dau, F. The Emergence of Spin Electronics in Data Storage. *Nat. Mater.* **2007**, *6*, 813−823.

(2) Khvalkovskiy, A. V.; Apalkov, D.; Watts, S.; Chepulskii, R.; Beach, R. S.; Ong, A.; Tang, X.; Driskill-Smith, A.; Butler, W. H.; Visscher, P. B.; Lottis, D.; Chen, E.; Nikitin, V.; Krounbi, M. Basic Principles of STT-MRAM Cell Operation in Memory Arrays. *J. Phys. D: Appl. Phys.* **2013**, *46*, 074001.

(3) Kent, A. D.; Worledge, D. C. A New Spin on Magnetic Memories. *Nat. Nanotechnol.* **2015**, *10*, 187−191.

(4) Dieny, B.; Prejbeanu, I. L.; Garello, K.; Gambardella, P.; Freitas, P.; Lehndorff, R.; Raberg, W.; Ebels, U.; Demokritov, S. O.; Akerman, J.; Deac, A.; Pirro, P.; Adelmann, C.; Anane, A.; Chumak, A.; Hiroata, A.; Mangin, S.; Onbasli, M. C.; D'Aquino, M.; Prenat, G.; et al. Opportunities and Challenges for Spintronics in the Microelectronic Industry. *arXiv:1908.10584*, **2019**. https://arxiv.org/abs/1908.10584 (November 17, 2019).

(5) Behin-Aein, B.; Datta, D.; Salahuddin, S.; Datta, S. Proposal for an All-Spin Logic Device with Built-in Memory. *Nat. Nanotechnol.* **2010**, *5*, 266−270.

(6) Manipatruni, S.; Nikonov, D. E.; Lin, C. C.; Gosavi, T. A.; Liu, H.; Prasad, B.; Huang, Y. L.; Bonturim, E.; Ramesh, R.; Young, I. A. Scalable Energy-Efficient Magnetoelectric Spin-Orbit Logic. *Nature* **2019**, *565*, 35−42.

(7) Torrejon, J.; Riou, M.; Araujo, F. A.; Tsunegi, S.; Khalsa, G.; Querlioz, D.; Bortolotti, P.; Cros, V.; Yakushiji, K.; Fukushima, A.; Kubota, H.; Yuasa, S.; Stiles, M. D.; Grollier, J. Neuromorphic Computing with Nanoscale Spintronic Oscillators. *Nature* **2017**, *547*, 428−431.

(8) Mizrahi, A.; Hirtzlin, T.; Fukushima, A.; Kubota, H.; Yuasa, S.; Grollier, J.; Querlioz, D. Neural-Like Computing with Populations of Superparamagnetic Basis Functions. *Nat. Commun.* **2018**, *9*, 1533.

(9) Borders, W. A.; Pervaiz, A. Z.; Fukami, S.; Camsari, K. Y.; Ohno, H.; Datta, S. Integer Factorization Using Stochastic Magnetic Tunnel Junctions. *Nature* **2019**, *573*, 390−393.

(10) De Teresa, J. M.; Barthélémy, A.; Fert, A.; Contour, J. P.; Montaigne, F.; Seneor, P. Role of Metal-Oxide Interface in Determining the Spin Polarization of Magnetic Tunnel Junctions. *Science* **1999**, *286*, 507−509.

(11) Piquemal-Banci, M.; Galceran, R.; Martin, M. B.; Godel, F.; Anane, A.; Petroff, F.; Dlubak, B.; Seneor, P. 2D-MTJs: Introducing 2D Materials in Magnetic Tunnel Junctions. *J. Phys. D: Appl. Phys.* **2017**, *50*, 203002.

(12) Rougemaille, N.; Ndiaye, A. T.; Coraux, J.; Vo-Van, C.; Fruchart, O.; Schmid, A. K. Perpendicular Magnetic Anisotropy of Cobalt Films Intercalated under Graphene. *Appl. Phys. Lett.* **2012**, *101*, 142403.

(13) Roche, S.; Åkerman, J.; Beschoten, B.; Charlier, J. C.; Chshiev, M.; Dash, S. P.; Dlubak, B.; Fabian, J.; Fert, A.; Guimarães, M.; Guinea, F.; Grigorieva, I.; Schönenberger, C.; Seneor, P.; Stampfer, C.; Valenzuela, S. O.; Waintal, X.; Van Wees, B. Graphene Spintronics: The European Flagship Perspective. *2D Mater.* **2015**, *2*, 030202.

(14) Han, W.; Kawakami, R. K.; Gmitra, M.; Fabian, J. Graphene Spintronics. *Nat. Nanotechnol.* **2014**, *9*, 794−807.

(15) Lv, W.; Jia, Z.; Wang, B.; Lu, Y.; Luo, X.; Zhang, B.; Zeng, Z.; Liu, Z. Electric-Field Control of Spin-Orbit Torques in WS_2/Permalloy Bilayers. *ACS Appl. Mater. Interfaces* **2018**, *10*, 2843−2849.

(16) Cobas, E.; Friedman, A. L.; Van'T Erve, O. M. J.; Robinson, J. T.; Jonker, B. T. Graphene as a Tunnel Barrier: Graphene-Based Magnetic Tunnel Junctions. *Nano Lett.* **2012**, *12*, 3000−3004.

(17) Martin, M. B.; Dlubak, B.; Weatherup, R. S.; Piquemal-Banci, M.; Yang, H.; Blume, R.; Schloegl, R.; Collin, S.; Petroff, F.; Hofmann, S.; Robertson, J.; Anane, A.; Fert, A.; Seneor, P. Protecting Nickel with Graphene Spin-Filtering Membranes: A Single Layer Is Enough. *Appl. Phys. Lett.* **2015**, *107*, 012408.

(18) Chen, J. J.; Meng, J.; Zhou, Y. B.; Wu, H. C.; Bie, Y. Q.; Liao, Z. M.; Yu, D. P. Layer-by-Layer Assembly of Vertically Conducting Graphene Devices. *Nat. Commun.* **2013**, *4*, 1921−1927.

(19) Dankert, A.; Venkata Kamalakar, M.; Wajid, A.; Patel, R. S.; Dash, S. P. Tunnel Magnetoresistance with Atomically Thin Two-Dimensional Hexagonal Boron Nitride Barriers. *Nano Res.* **2015**, *8*, 1357−1364.

(20) Piquemal-Banci, M.; Galceran, R.; Godel, F.; Caneva, S.; Martin, M. B.; Weatherup, R. S.; Kidambi, P. R.; Bouzehouane, K.; Xavier, S.; Anane, A.; Petroff, F.; Fert, A.; Dubois, S. M. M.; Charlier, J. C.; Robertson, J.; Hofmann, S.; Dlubak, B.; Seneor, P. Insulator-to-Metallic Spin-Filtering in 2D-Magnetic Tunnel Junctions Based on Hexagonal Boron Nitride. *ACS Nano* **2018**, *12*, 4712−4718.

(21) Piquemal-Banci, M.; Galceran, R.; Caneva, S.; Martin, M. B.; Weatherup, R. S.; Kidambi, P. R.; Bouzehouane, K.; Xavier, S.; Anane, A.; Petroff, F.; Fert, A.; Robertson, J.; Hofmann, S.; Dlubak, B.; Seneor, P. Magnetic Tunnel Junctions with Monolayer Hexagonal Boron Nitride Tunnel Barriers. *Appl. Phys. Lett.* **2016**, *108*, 102404.

(22) Hashimoto, T.; Kamikawa, S.; Soriano, D.; Pedersen, J. G.; Roche, S.; Haruyama, J. Tunneling Magnetoresistance Phenomenon Utilizing Graphene Magnet Electrode. *Appl. Phys. Lett.* **2014**, *105*, 183111.

(23) Karpan, V. M.; Giovannetti, G.; Khomyakov, P. A.; Talanana, M.; Starikov, A. A.; Zwierzycki, M.; Van Den Brink, J.; Brocks, G.; Kelly, P. J. Graphite and Graphene as Perfect Spin Filters. *Phys. Rev. Lett.* **2007**, *99*, 176602.

(24) Zibouche, N.; Kuc, A.; Musfeldt, J.; Heine, T. Transition-Metal Dichalcogenides for Spintronic Applications. *Ann. Phys.* **2014**, *526*, 395−401.

(25) Ulstrup, S.; Čabo, A. G.; Biswas, D.; Riley, J. M.; Dendzik, M.; Sanders, C. E.; Bianchi, M.; Cacho, C.; Matselyukh, D.; Chapman, R. T.; Springate, E.; King, P. D. C.; Miwa, J. A.; Hofmann, P. Spin and Valley Control of Free Carriers in Single-Layer WS_2. *Phys. Rev. B: Condens. Matter Mater. Phys.* **2017**, *95*, 1−5.

(26) Tanabe, I.; Gomez, M.; Coley, W. C.; Le, D.; Echeverria, E. M.; Stecklein, G.; Kandyba, V.; Balijepalli, S. K.; Klee, V.; Nguyen, A. E.; Preciado, E.; Lu, I. H.; Bobek, S.; Barroso, D.; Martinez-Ta, D.; Barinov, A.; Rahman, T. S.; Dowben, P. A.; Crowell, P. A.; Bartels, L. Band Structure Characterization of WS_2 Grown by Chemical Vapor Deposition. *Appl. Phys. Lett.* **2016**, *108*, 252103.

(27) Yun, W. S.; Han, S. W.; Hong, S. C.; Kim, I. G.; Lee, J. D. Thickness and Strain Effects on Electronic Structures of Transition Metal Dichalcogenides: 2H-MX_2 Semiconductors (M = Mo, W; X = S, Se, Te). *Phys. Rev. B: Condens. Matter Mater. Phys.* **2012**, *85*, 033305.

(28) Peimyoo, N.; Yang, W.; Shang, J.; Shen, X.; Wang, Y.; Yu, T. Chemically Driven Tunable Light Emission of Charged and Neutral Excitons in Monolayer WS_2. *ACS Nano* **2014**, *8*, 11320−11329.

DOI: 10.1021/acsnano.9b08178
ACS Nano 2019, 13, 14468−14476

(29) Latzke, D. W.; Zhang, W.; Suslu, A.; Chang, T. R.; Lin, H.; Jeng, H. T.; Tongay, S.; Wu, J.; Bansil, A.; Lanzara, A. Electronic Structure, Spin-Orbit Coupling, and Interlayer Interaction in Bulk MoS_2 and WS_2. *Phys. Rev. B: Condens. Matter Mater. Phys.* **2015**, *91*, 235202.
(30) Kuc, A.; Zibouche, N.; Heine, T. Influence of Quantum Confinement on the Electronic Structure of the Transition Metal Sulfide TS_2. *Phys. Rev. B: Condens. Matter Mater. Phys.* **2011**, *83*, 245213.
(31) Klein, A.; Tiefenbacher, S.; Eyert, V.; Pettenkofer, C.; Jaegermann, W. Electronic Band Structure of Single-Crystal and Single-Layer WS_2: Influence of Interlayer van der Waals Interactions. *Phys. Rev. B: Condens. Matter Mater. Phys.* **2001**, *64*, 205416.
(32) Zhao, W.; Ghorannevis, Z.; Chu, L.; Toh, M.; Kloc, C.; Tan, P. H.; Eda, G. Evolution of Electronic Structure in Atomically Thin Sheets of WS_2 and WSe_2. *ACS Nano* **2013**, *7*, 791−797.
(33) Wang, W.; Narayan, A.; Tang, L.; Dolui, K.; Liu, Y.; Yuan, X.; Jin, Y.; Wu, Y.; Rungger, I.; Sanvito, S.; Xiu, F. Spin-Valve Effect in NiFe/MoS_2/NiFe Junctions. *Nano Lett.* **2015**, *15*, 5261−5267.
(34) Galbiati, M.; Vecchiola, A.; Mañas-Valero, S.; Canet-Ferrer, J.; Galceran, R.; Piquemal-Banci, M.; Godel, F.; Forment-Aliaga, A.; Dlubak, B.; Seneor, P.; Coronado, E. A Local Study of the Transport Mechanisms in MoS_2 Layers for Magnetic Tunnel Junctions. *ACS Appl. Mater. Interfaces* **2018**, *10*, 30017−30021.
(35) Dankert, A.; Pashaei, P.; Kamalakar, M. V.; Gaur, A. P. S.; Sahoo, S.; Rungger, I.; Narayan, A.; Dolui, K.; Hoque, M. A.; Patel, R. S.; De Jong, M. P.; Katiyar, R. S.; Sanvito, S.; Dash, S. P. Spin-Polarized Tunneling through Chemical Vapor Deposited Multilayer Molybdenum Disulfide. *ACS Nano* **2017**, *11*, 6389−6395.
(36) Wong, W.; Ng, S.; Wong, H.; Cheng, W.; Mak, C.; Leung, C. Spin-Valve Junction with Transfer-Free MoS_2 Spacer Prepared by Sputtering. *2017 IEEE* **2017**, *53*, 1−5.
(37) Wu, H. C.; Coileáin, C.; Abid, M.; Mauit, O.; Syrlybekov, A.; Khalid, A.; Xu, H.; Gatensby, R.; Jing Wang, J.; Liu, H.; Yang, L.; Duesberg, G. S.; Zhang, H. Z.; Abid, M.; Shvets, I. V. Spin-Dependent Transport Properties of Fe_3O_4/MoS_2/Fe_3O_4 Junctions. *Sci. Rep.* **2015**, *5*, 1−8.
(38) Dankert, A.; Dash, S. P. Electrical Gate Control of Spin Current in van der Waals Heterostructures at Room Temperature. *Nat. Commun.* **2017**, *8*, 16093.
(39) Safeer, C. K.; Ingla-Aynés, J.; Herling, F.; Garcia, J. H.; Vila, M.; Ontoso, N.; Calvo, M. R.; Roche, S.; Hueso, L. E.; Casanova, F. Room-Temperature Spin Hall Effect in Graphene/MoS_2 van der Waals Heterostructures. *Nano Lett.* **2019**, *19*, 1074−1082.
(40) Marinov, K.; Avsar, A.; Watanabe, K.; Taniguchi, T.; Kis, A. Resolving the Spin Splitting in the Conduction Band of Monolayer MoS_2. *Nat. Commun.* **2017**, *8*, 1938.
(41) Iqbal, M. Z.; Iqbal, M. W.; Siddique, S.; Khan, M. F.; Ramay, S. M. Room Temperature Spin Valve Effect in NiFe/WS_2/Co Junctions. *Sci. Rep.* **2016**, *6*, 2−7.
(42) O'Farrell, E. C. T.; Avsar, A.; Tan, J. Y.; Eda, G.; Ozyilmaz, B. Quantum Transport Detected by Strong Proximity Interaction at a Graphene-WS_2 van der Waals Interface. *Nano Lett.* **2015**, *15*, 5682−5688.
(43) Ghiasi, T. S.; Ingla-Aynés, J.; Kaverzin, A. A.; Van Wees, B. J. Large Proximity-Induced Spin Lifetime Anisotropy in Transition-Metal Dichalcogenide/Graphene Heterostructures. *Nano Lett.* **2017**, *17*, 7528−7532.
(44) Cummings, A. W.; Garcia, J. H.; Fabian, J.; Roche, S. Giant Spin Lifetime Anisotropy in Graphene Induced by Proximity Effects. *Phys. Rev. Lett.* **2017**, *119*, 206601.
(45) Omar, S.; Van Wees, B. J. Spin Transport in High-Mobility Graphene on WS_2 Substrate with Electric-Field Tunable Proximity Spin-Orbit Interaction. *Phys. Rev. B: Condens. Matter Mater. Phys.* **2018**, *97*, 045414.
(46) Dastgeer, G.; Khan, M. F.; Nazir, G.; Afzal, A. M.; Aftab, S.; Akbar, K.; Chun, S. H.; Eom, J. Surface Spin Accumulation Due to the Inverse Spin Hall Effect in WS_2 Crystals. *2D Mater.* **2019**, *6*, 011007.
(47) Benítez, L. A.; Sierra, J. F.; Savero Torres, W.; Arrighi, A.; Bonell, F.; Costache, M. V.; Valenzuela, S. O. Strongly Anisotropic Spin Relaxation in Graphene-Transition Metal Dichalcogenide Heterostructures at Room Temperature. *Nat. Phys.* **2018**, *14*, 303−308.
(48) Jiang, H. Electronic Band Structures of Molybdenum and Tungsten Dichalcogenides by the GW Approach. *J. Phys. Chem. C* **2012**, *116*, 7664−7671.
(49) Scharf, B.; Xu, G.; Matos-Abiague, A.; Žutić, I. Magnetic Proximity Effects in Transition-Metal Dichalcogenides: Converting Excitons. *Phys. Rev. Lett.* **2017**, *119*, 127403.
(50) Yuan, H.; Bahramy, M. S.; Morimoto, K.; Wu, S.; Nomura, K.; Yang, B.-J.; Shimotani, H.; Suzuki, R.; Toh, M.; Kloc, C.; Xu, X.; Arita, R.; Nagaosa, N.; Iwasa, Y. Zeeman-Type Spin Splitting Controlled by an Electric Field. *Nat. Phys.* **2013**, *9*, 563−569.
(51) Dolui, K.; Narayan, A.; Rungger, I.; Sanvito, S. Efficient Spin Injection and Giant Magnetoresistance in Fe/MoS_2/Fe Junctions. *Phys. Rev. B: Condens. Matter Mater. Phys.* **2014**, *90*, 041401.
(52) Zhou, J.; Qiao, J.; Duan, C. G.; Bournel, A.; Wang, K. L.; Zhao, W. Large Tunneling Magnetoresistance in VSe_2 /MoS_2 Magnetic Tunnel Junction. *ACS Appl. Mater. Interfaces* **2019**, *11*, 17647−17653.
(53) Reale, F.; Palczynski, P.; Amit, I.; Jones, G. F.; Mehew, J. D.; Bacon, A.; Ni, N.; Sherrell, P. C.; Agnoli, S.; Craciun, M. F.; Russo, S.; Mattevi, C. High-Mobility and High-Optical Quality Atomically Thin WS_2. *Sci. Rep.* **2017**, *7*, 1−10.
(54) Tsymbal, E. Y.; Mryasov, O. N.; LeClair, P. R. Spin-Dependent Tunnelling in Magnetic Tunnel Junctions. *J. Phys.: Condens. Matter* **2003**, *15*, R109.
(55) Žutic, I.; Fabian, J.; Das Sarma, S. Spintronics: Fundamentals and Applications. *Rev. Mod. Phys.* **2004**, *76*, 323.
(56) Bernand-Mantel, A.; Seneor, P.; Lidgi, N.; Muñoz, M.; Cros, V.; Fusil, S.; Bouzehouane, K.; Deranlot, C.; Vaures, A.; Petroff, F.; Fert, A. Evidence for Spin Injection in a Single Metallic Nanoparticle: A Step towards Nanospintronics. *Appl. Phys. Lett.* **2006**, *89*, 062502.
(57) Barraud, C.; Deranlot, C.; Seneor, P.; Mattana, R.; Dlubak, B.; Fusil, S.; Bouzehouane, K.; Deneuve, D.; Petroff, F.; Fert, A. Magnetoresistance in Magnetic Tunnel Junctions Grown on Flexible Organic Substrates. *Appl. Phys. Lett.* **2010**, *96*, 072502.
(58) Berkdemir, A.; Gutiérrez, H. R.; Botello-Méndez, A. R.; Perea-López, N.; Elías, A. L.; Chia, C. I.; Wang, B.; Crespi, V. H.; López-Urías, F.; Charlier, J. C.; Terrones, H.; Terrones, M. Identification of Individual and Few Layers of WS_2 Using Raman Spectroscopy. *Sci. Rep.* **2013**, *3*, 1−8.
(59) Mzali, S.; Montanaro, A.; Xavier, S.; Servet, B.; Mazellier, J. P.; Bezencenet, O.; Legagneux, P.; Piquemal-Banci, M.; Galceran, R.; Dlubak, B.; Seneor, P.; Martin, M. B.; Hofmann, S.; Robertson, J.; Cojocaru, C. S.; Centeno, A.; Zurutuza, A. Stabilizing a Graphene Platform toward Discrete Components. *Appl. Phys. Lett.* **2016**, *109*, 253110.
(60) Galceran, R.; Gaufres, E.; Loiseau, A.; Piquemal-Banci, M.; Godel, F.; Vecchiola, A.; Bezencenet, O.; Martin, M. B.; Servet, B.; Petroff, F.; Dlubak, B.; Seneor, P. Stabilizing Ultra-Thin Black Phosphorus with *In-Situ* -Grown 1 nm-Al_2O_3 Barrier. *Appl. Phys. Lett.* **2017**, *111*, 243101.
(61) Galbiati, M.; Tatay, S.; Dubois, S. M.-M.; Godel, F.; Galceran, R.; Mañas-Valero, S.; Piquemal-Banci, M.; Vecchiola, A.; Charlier, J.-C.; Forment-Aliaga, A.; Coronado, E.; Dlubak, B.; Seneor, P. Path to Overcome Material and Fundamental Obstacles in Spin Valves Based on MoS_2 and Other Transition-Metal Dichalcogenides. *Phys. Rev. Appl.* **2019**, *12*, 044022.
(62) Terrones, H.; Del Corro, E.; Feng, S.; Poumirol, J. M.; Rhodes, D.; Smirnov, D.; Pradhan, N. R.; Lin, Z.; Nguyen, M. A. T.; Elías, A. L.; Mallouk, T. E.; Balicas, L.; Pimenta, M. A.; Terrones, M. N. First Order Raman-Active Modes in Few Layered Transition Metal Dichalcogenides. *Sci. Rep.* **2015**, *4*, 4215.
(63) McCreary, A.; Berkdemir, A.; Wang, J.; Nguyen, M. A.; Elías, A. L.; Perea-López, N.; Fujisawa, K.; Kabius, B.; Carozo, V.; Cullen, D. A.; Mallouk, T. E.; Zhu, J.; Terrones, M. Distinct Photoluminescence and Raman Spectroscopy Signatures for Identifying Highly Crystalline

WS_2 Monolayers Produced by Different Growth Methods. *J. Mater. Res.* **2016**, *31*, 931−944.
(64) Julliere, M. Tunneling between Ferromagnetic Films. *Phys. Lett. A* **1975**, *54*, 225−226.
(65) Zeng, H.; Liu, G.-B.; Dai, J.; Yan, Y.; Zhu, B.; He, R.; Xie, L.; Xu, S.; Chen, X.; Yao, W.; Cui, X. Optical Signature of Symmetry Variations and Spin-Valley Coupling in Atomically Thin Tungsten Dichalcogenides. *Sci. Rep.* **2013**, *3*, 1608.
(66) Martin, M. B.; Dlubak, B.; Weatherup, R. S.; Yang, H.; Deranlot, C.; Bouzehouane, K.; Petroff, F.; Anane, A.; Hofmann, S.; Robertson, J.; Fert, A.; Seneor, P. Sub-Nanometer Atomic Layer Deposition for Spintronics in Magnetic Tunnel Junctions Based on Graphene Spin-Filtering Membranes. *ACS Nano* **2014**, *8*, 7890−7895.
(67) Kresse, G.; Hafner, J. *Ab Initio* Molecular Dynamics for Liquid Metals. *Phys. Rev. B: Condens. Matter Mater. Phys.* **1993**, *47*, 558−561.
(68) Kresse, G.; Joubert, D. From Ultrasoft Pseudopotentials to the Projector Augmented-Wave Method. *Phys. Rev. B: Condens. Matter Mater. Phys.* **1999**, *59*, 1758−1775.
(69) Perdew, J. P.; Burke, K.; Ernzerhof, M. Generalized Gradient Approximation Made Simple. *Phys. Rev. Lett.* **1996**, *77*, 3865−3868.

DOI: 10.1021/acsnano.9b08178
ACS Nano 2019, 13, 14468−14476